Comparison of the Impact of Moisture on Methane Adsorption and Nanoporosity for Over Mature Shales and their Kerogens

Wei Li[a], Lee A. Stevens[a], Clement N. Uguna[a], Christopher H. Vane[b], Will Meredith[a], Ling Tang[c], Qianwen Li[d], Colin E. Snape*[a]

a. University of Nottingham, Low Carbon Energy and Resources Technologies Group, Faculty of Engineering, Energy Technologies Building, Triumph Road, Nottingham NG7 2TU, UK.
b. British Geological Survey, Centre for Environmental Geochemistry, Keyworth, Nottingham NG12 5GG, UK.
c. State Key Laboratory of Petroleum Resources and Prospecting, China University of Petroleum, Beijing 102249, China.
d. Sinopec Petroleum Exploration and Production Research Institute, Beijing 100083, China.

* Corresponding author, Colin.Snape@nottingham.ac.uk

Abstract

Moisture in shales under reservoir conditions adversely affects gas adsorption and nanoporosity and is also likely to impact on the contribution that kerogen makes to the methane adsorption capacity. To investigate these phenomena, two over mature shales from the Wufeng-Longmaxi Formation, and their kerogens isolated by demineralisation were investigated at dry and 95% relative humidity (R.H.) by high-pressure methane adsorption, and low-pressure nitrogen (N_2) and carbon dioxide (CO_2) sorption. The kerogen concentrates account for 68-97% and 50-64% of the methane adsorption capacities for the shales dry and at 95% R.H. respectively. However, the isolated kerogens could adsorb more methane than the organic matter in the shales because their shallower adsorption isotherms indicate large micropores and small mesopores not evident for the shales. Methane adsorption capacities of the kerogens and shales reduced by 46-72% at 95% R.H.. This compares with the reductions in surface area (SA) and pore volume of 81% and 48-59%, respectively, for the kerogens and 98-99% for both SA and pore volume of the shales at 95% R.H.. Water can block most micropores less than 1.3 nm reducing the micropores volume and blocking the micropore necks connecting the larger pores, and vastly reducing accessible pores for gas transport. The greater proportional losses in SA and pore volume compared to the methane adsorption capacities is probably due to ice forming at -196 °C in the low-pressure N_2 analysis. Not taking

moisture into account for estimating free and adsorbed methane results can overestimate the total gas in place (GIP) by 36-45% for the shales investigated.

Keywords: Kerogen; Moisture; Methane Adsorption Capacity; Nanoporosity.

1. Introduction

Shale gas is stored in adsorbed, free and dissolved states and it is often estimated from the sum of the adsorbed and free gas in the pores (Chen et al., 2017; Curtis, 2002; Jarvie et al., 2007; Rexer et al., 2014; Ross and Bustin, 2008). The adsorbed gas is significant under reservoir conditions, estimated as 20-85% of the total gas in organic-rich shales (Adesida et al., 2011; Curtis, 2002; Heller and Zoback, 2014; Ross and Bustin, 2008). Kerogen, the organic matter insoluble in alkali, non-oxidizing acids and organic solvents in shales (Durand, 1980; Hunt, 1979), is considered to store much of the gas since methane adsorption capacity of shale generally increases with increasing total organic content (TOC) (Gasparik et al., 2014; Ross and Bustin, 2009; Zhang et al., 2012). In addition to the kerogen, the major minerals in shales including quartz, clays and calcite are also believed to provide porosity for shale gas to adsorb in different extents (Gasparik et al., 2014; Gasparik et al., 2012; Loucks et al., 2012; Ma et al., 2017; Peng et al., 2020; Peng et al., 2019; Ross and Bustin, 2009). Gasparik (2012) reported no correlation between TOC and dry adsorption capacity for some shales, suggesting that the sorption capacities of the minerals can be significant.

To investigate methane adsorption on isolated kerogens, Hu (2014) chose two kerogens of different maturity (vitrinite reflectance (VR) of 0.58 and 2.01% Ro), and found that the more mature kerogen had a much higher adsorption capacity. Methane adsorption experiments on organic-rich shales and their isolated kerogens were conducted at different temperatures under dry conditions to study the impact of different parameters on gas adsorption but not including moisture (Li et al., 2018; Rexer et al., 2014; Zhang et al., 2012). Fan (2014) found that 43-57% of the methane adsorption in dry shales was accounted for by the kerogen, confirming that kerogen has a much larger methane adsorption capacity than minerals. Rexer et al (2014) compared kerogen and shale using low-pressure nitrogen (N_2) and carbon dioxide (CO_2) and high-pressure methane isotherms and identified that the vast majority sorption of methane occurs in the pores less than 6 nm, and kerogen accounts for about 50% total measured adsorbed methane in dry shales investigated. Although these studies confirm that kerogen accounts for much of the methane adsorption capacity in shale, the impact of moisture present has not been addressed.

Moisture always exists under reservoirs conditions and has a profound negative influence on gas adsorption capacity (Heller and Zoback, 2014; Ji et al., 2012; Jin and Firoozabadi, 2014;

Zolfaghari et al., 2017b). Some studies have addressed the impact of moisture on methane adsorption for shales and coals (Gasparik et al., 2014; Joubert et al., 1973; Ross and Bustin, 2007; Whitelaw et al., 2019; Zou et al., 2018). Joubert (1973) found methane adsorption capacity for coals decreased with increasing humidity, although there was a "critical value" of moisture above which no change in adsorption capacity occurred. High critical values were thought to relate to high coal oxygen contents since there is a strong interaction between the polar water molecule and the surface oxygen complexes (Day et al., 2008; Joubert et al., 1973). The critical moisture content of shale is approximately 75% R.H. (Gasparik et al., 2014). Ross and Bustin (2007) compared the isotherms of dry shales with moisture equilibrated shales from the Lower Jurassic Gordondale Member and showed that methane adsorbed in dry shales (0.5–4.0 cm^3/g) were much larger than that in moisture equilibrated shales (0.1–1.6 cm^3/g). Reductions of 20-85% in methane adsorption capacities have also been reported by Merkel (2016) and Whitelaw et al (2019) at high R.H., the latter finding that moisture reduced pore volume by over 90%. In contrast, Zou (2018) reported much smaller reductions of less than 20% in methane adsorption capacity and 30% in pore volume because their degassing of the 84% R.H. shales and standardised pre-evacuation procedures for the low and high-pressure instruments is likely to have removed any free and weakly adsorbed water, resulting in the moisture being considerably less than 84% R.H. when the experiments started. Moisture adsorbed on hydrophilic clay minerals is considered to be main reason for the decreasing methane adsorption in a number of studies (Heller and Zoback, 2014; Jin and Firoozabadi, 2014; Liming et al., 2012a; Zolfaghari et al., 2017a; Zou et al., 2018).

Methane adsorption in shale and kerogen is clearly related to pore structure (Li et al., 2019; Liming et al., 2012b; Rexer et al., 2014). Molecular simulation was used to study the impact of different pore sizes on methane adsorption and other gases (e.g. CO_2, N_2) in kerogen (Huang et al., 2018; Xiong et al., 2017; Zhao et al., 2018). In addition to molecular simulation, some experimental studies on kerogens have focused on methane adsorption, but without investigating the pore size distribution (PSD) (Fan et al., 2014; Hu, 2014; Li et al., 2018; Pang et al., 2019; Zhang et al., 2012). Other studies have only addressed pore characterization without considering methane adsorption (Adesida et al., 2011; Cao et al., 2015; Chen et al., 2013; Ji et al., 2017; Liu et al., 2018). Only a few studies (Rexer et al., 2014; Xiong et al., 2017) have investigated both methane adsorption and pore structure but only under dry conditions.

This study is the first to relate methane adsorption capacities and pore characteristics of shales and their isolated kerogens, both dry and equilibrated at 95% R.H., and to compare the impact of moisture on methane adsorption capacity and nanoporosity for kerogens and shales. Furthermore, this research provides new guidance on accounting for moisture to estimate gas in place (GIP) for shales. This is often estimated from the total amount of free gas obtained from the total porosity and adsorbed gas content measured from methane adsorption (Li et al., 2018; Tang et al., 2016). GIP based on the accessible pore volume and methane adsorption of dry shales without taking moisture into account is overestimated (Li et al., 2018; Tang et al., 2016), since moisture exists in shale reservoirs (Feng et al., 2018; Loucks and Ruppel, 2007; Merkel et al., 2015).

2. Methods

2.1 Sample preparation

2.1.1 Kerogen isolation Two over mature shale samples, Shale 1 (SH1) and Shale 2 (SH2) from a depth of 4119 and 4098 m in the Wufeng-Longmaxi Formation, Sichuan Basin, China were selected for kerogen isolation. Shales from this formation and depth are considered as over matured as reported in previous studies (Dong et al., 2018; Dongjun et al., 2016; Fan et al., 2014). The two kerogen concentrates, K1 and K2 isolated from SH1 and SH2 were prepared by standard demineralisation procedures (Guthrie and Pratt, 1994; Rexer et al., 2014). Shale samples (60 g each) crushed into powder and treated with 37% hydrochloric acid (HCl) for 12 hours to remove carbonates. The HCl treated shales were washed with distilled water before using 40% hydrofluoric acid treatment for 48 hours to remove aluminosilicate minerals (Guthrie and Pratt, 1994). After decanting the acid, the powdered residue was then repeatedly washed six times with distilled water to remove the acid and reach pH 7. Samples were then freeze-dried (−5 °C) for 6 hours and dried at ambient temperature. After drying, 7.21 and 6.55 g of K1 and K2 were obtained respectively from 60 g of shale, and the yield of kerogen concentrate can be calculated.

2.1.2 Moisture-equilibration method The adsorption capacity of shale is influenced by particle size, where milling can destroy or create pores in shale (Gasparik et al., 2014; Rexer et al., 2014). Thus, shale samples were crushed into particles with a size range of 2-4 mm (10-5 mesh), but not to powders so as not to disrupt the interconnectivity between macro, meso and micropores (Whitelaw et al., 2019). The kerogen concentrates were in powder form after isolation with a particle size <250 µm. The shales and kerogen concentrates were first dried at 120 °C in a vacuum oven (<0.5 mbar) for 48 hours to get the dry sample and dry mass. Then, the 95% R.H. moisture equilibrated (wet) samples were prepared in a vacuum desiccator containing saturated potassium nitrate (KNO_3) solution (8 g KNO_3/10 mL H_2O) at a controlled temperature of 20 °C for 48 hours (Young, 1967; Zolfaghari et al., 2017a). A logger in the desiccator was used to monitor the R.H. and the temperature. The moisture content for the wet samples were calculated from the mass difference (equation (1)) of equilibrated 'wet' samples and after drying under vacuum. The water volume uptake in shales at 95 % R.H. are calculated from the moisture contents and densities by equation (2).

$$W = \frac{M_{water}}{M_{dry}} \quad (1)$$

$$S_w = \frac{V_{water}}{V_{dry\ pore}} = 1 - \frac{\rho_{dry\ sk}}{\rho_{dry\ sk} - \rho_{dry\ bulk}} + \frac{\rho_{dry\ sk} \times \rho_{dry\ bulk} \times (1+W)}{\rho_{wet\ sk} \times (\rho_{dry\ sk} - \rho_{dry\ bulk})} \quad (2)$$

Where, W is the moisture content, M_{dry} is the mass of dry sample, M_{water} is the mass of the water, S_w is the water volume uptake, V_{water} is the volume of the water in pore, $V_{dry\ pore}$ is the total pore volume in dry sample, $\rho_{dry\ bulk}$ is the bulk density of the dry sample from mercury intrusion porosimetry (MIP) at 0.03 bar, $\rho_{dry\ sk}$ and $\rho_{wet\ sk}$ are the skeletal densities of the dry and wet samples obtained from helium pycnometry.

2.2 Elemental analysis and X-ray diffraction

TOC contents were determined using Leco CHN628 instruments. Up to 3 g of the powdered shales (<250 μm) were treated using HCl with a concentration of 1 mol/L for 24 hours to remove carbonates. The samples were then washed with distilled water 6 times to remove the acid and reach pH 7. After carefully decanting the water from the samples, the samples were dried in the vacuum oven (<0.5 mbar) for 48 hrs at 120 °C. The TOC contents were measured using 120 mg shale and 75 mg kerogen, respectively. All the elemental analyses were carried out in triplicate. X-ray diffraction (XRD) method was used to determine the relative mineral phases using a Rigaku D/max-2500PC instrument, before testing, all samples were ground into less than 0.04 mm, detail procedure was described in Tang (2019).

2.3 Field emission scanning electron microscopy (FE-SEM)

The shales were analysed where one side surface of the selected sample was polished by argon-ion to get a smooth surface using a Leica EM TIC020 mill with an accelerating voltage of 8 kV, current of 2.8 mA for about 8 hours. Then, the samples were coated with a 25 nm conductive layer by the PELCO conductive carbon paste. The samples were imaged using a JSM-6700F FE-SEM, all the high-resolution FE-SEM images were processed using Image J-1.53a software (Abràmoff et al., 2004).

2.4 High-pressure methane adsorption

High-pressure methane adsorption measurements were performed using a Particulate Systems High-Pressure Volumetric Analyzer (HPVA-100) designed to obtain high-pressure sorption isotherms employing the static volumetric method (pressures up to 105 bar and temperatures up to 500 °C). Approximately 10 g of moisture equilibrated shale (2-4 mm) and 3 g of moisture equilibrated powder kerogen concentrate (<250 μm) were weighed and

loaded into the 10 mL stainless steel sample cell and sealed. For wet samples, the methane adsorption isotherms were acquired from 1.2 to 105 bar at 25 °C, avoiding samples being subjected to a vacuum on the high-pressure instrument. The mass deviation of wet samples before and after analysis was less than ±0.0018%, verifying the moisture is still in the sample. For dry adsorption isotherms, the samples were degassed at 120 °C for 48 hours before starting the methane adsorption method. A sample pre-evacuation was carried out for 45 minutes to reach a vacuum setpoint of 0.013 bar on the high-pressure instrument and an isotherm was generated from 0 to 105 bar. Similar free space corrections were carried out on this instrument as for the low-pressure gas sorption method (2.5).

Each sample was analysed in triplicate to assess errors. The excess adsorption quantity is obtained by the volumetric sorption measurement; therefore, it is necessary to convert to absolute adsorption quantity by Gibbs equation (equation (3)) (Sircar, 1999; Tang et al., 2016). The HPVA can measure the adsorption up to 105 bar, whereas, the adsorbed gas quantities at higher pressures can be predicted by the dual-site Langmuir model which is for heterogeneous adsorbents (Tang et al., 2016; Whitelaw et al., 2019). The equation for the dual-site Langmuir can be written in the following form (equation (4)), and equation (5) and (6) show the $b_1(T)$ and $b_2(T)$:

$$n_a = n_e + (V_a \times \rho_g) \quad (3)$$

$$n_a(P,T) = n_{max} \times \left[(1-\alpha)\frac{b_1(T)P}{1+b_1(T)P} + \alpha\frac{b_2(T)P}{1+b_2(T)P}\right] \quad (4)$$

$$b_1(T) = A_1 \times exp\left(-\frac{E_1}{RT}\right) \quad (5)$$

$$b_2(T) = A_2 \times exp\left(-\frac{E_2}{RT}\right) \quad (6)$$

Where, n_a is the absolute adsorption quantity; n_e is the excess adsorption quantity; V_a is the pore volume for gas to adsorb into; ρ_g is the density of the bulk gas; $n_{max}$is the maximum equilibrium adsorption quantity; $b_1(T)$ and $b_2(T)$ are the temperature-dependent equilibrium constants; $b_1(T)$ and $b_2(T)$ are weighted by a coefficient (α); α is the fraction of the second type of site ($0 < \alpha < 1$); E_1 and E_2 are the energy of adsorption of two sites; A_1 and A_2 are the pre-exponential coefficient; R is the ideal gas content, P is the pressure and T is the temperature.

2.5 Low-pressure gas sorption

Low-pressure gas sorption experiments were carried out for both dry and 95% R.H. moisture equilibrated (wet) samples by a Micromeritics Surface Area and Porosity Analyser (ASAP 2420). For shale samples, 4 g particles (2-4 mm) were used for the low-pressure N_2 sorption experiments, 2 g for CO_2 adsorption and about 1 g of the powdered kerogen concentrates (<250 μm) for both N_2 and CO_2 sorption. All the dry samples were degassed under high vacuum (<0.013 mbar) at 120 °C for 48 hours prior to analysis, and a pre-evacuation of 3 hours on the low-pressure instrument to reach the vacuum setpoint (0.013 bar) to start the isotherm. For low-pressure N_2 sorption, the prepared wet samples were frozen first in liquid N_2 for 30 minutes, before manually evacuating the sample tube and starting the analysis. This ensures moisture equilibrated samples are not exposed to vacuum at warmer temperatures on the low-pressure instrument. The mass deviation of wet samples before and after analysis was less than ±0.0020%, verifying the moisture still in the samples. The analysis for both dry and wet samples were performed in a liquid N_2 bath (-196 °C), with the relative pressure (P/P°, P is the absolute equilibrium pressure and P° is the saturation pressure) from 10^{-7} until 0.995 P/P°. CO_2 adsorption isotherms were acquired from 6×10^{-5} to 3.5×10^{-2} P/P° (absolute pressure is from 0.002 to 1.2 bar) at 0 °C to characterise the ultra-microporous structure (<0.8 nm) of dry shale and kerogen concentrates (Liu et al., 2015; Whitelaw et al., 2019). CO_2 adsorption was not carried out for wet samples because the experimental temperature is 0 °C which could not hold the moisture in the sample under low pressure. The SAs of dry samples obtained from N_2 and CO_2 show little difference suggesting N_2 can penetrate all ultra-micropores of both wet and dry samples.

Brunauer-Emmett-Teller (BET) theory was used to calculate the SA, where the P/P° between 0.05 and 0.2 of N_2 adsorption and P/P° between 0.025 and 0.030 of CO_2 adsorption were selected to get a positive BET 'C' parameter (Brunauer et al., 1938; Thommes et al., 2015). With the development of density functional theory and computer simulation approaches, the whole range of micro and mesopores can be probed with commercially available models such as Non-Local Density Functional Theory (NLDFT) (Qi et al., 2017; Rouquerol et al., 2007). NLDFT method based on the carbon slit pore model is applied to calculate the PSD from 0.33 to 100 nm in this study. Helium pycnometry was used to measure the skeletal density of wet and dry samples for the manual calculation of warm and cold free space to obtain exact gas

sorption results, as the free space test by helium cannot be used during the low-pressure gas sorption experiment, because an automatic warm free space test on the instrument would expose the moisture equilibrated samples to a vacuum which would remove the moisture.

2.6 Mercury intrusion porosimetry

A Micromeritics Autopore IV Series instrument was used to obtain the bulk density and the porosity of dry shale samples. 2 g shale (2-4 mm) samples were vacuumed dry at a temperature of 120 °C for 48 hours in a vacuum oven (<0.5 mbar) and loaded into a 5 ml solid penetrometer 0.366 ml internal volume, then sealed. The intrusion of mercury was recorded from 0-4137 bar. The volume of mercury entering the shale pores at a given pressure can be converted to pore volume and size using the Washburn equation for slit/angular shaped pores. A contact angle of 151.5° and a surface tension of 475.5 mN/m for mercury intrusion in shale was used to provide a pore size distribution from 231 μm to 2 nm (Wang et al., 2016). Correction methods were applied by running a blank penetrometer to remove any intrusion detected from an empty penetrometer (Malik et al., 2016).

3. Results and discussion

3.1 TOC, mineral compositions, and moisture content

Table 1. TOC, mineral compositions and moisture contents of the shales.

Sample Name	Moisture (Wt.%)	TOC(Wt.%)	Yield (wt.%)	Mineral (%)					
				Clay	Quartz	Plagioclase	Calcite	Dolomite	Pyrite
SH1	1.48±0.14	5.1±0.1	-	18.4	55.4	3.1	4	14.9	4.1
SH2	1.22±0.10	2.4±0.1	-	35.8	41.7	6.9	4.4	6.9	4.3
K1	15.5±2.9	36.3±1.4	12.0						
K2	13.0±1.2	18.7±0.2	10.9						

The mean of moisture content and TOC are from triplicate experiments (2.1.2) and (2.2), and the errors represent the dispersion of a dataset relative to its mean.

The compositions and physical properties of the two shales and their isolated kerogen concentrates are presented in Table 1. SH1 (5.1%) has a higher TOC than SH2 (2.4%). Combining the kerogen concentrate yields for SH1 and SH2 of 12.0 and 10.9 wt.%, respectively, with TOCs of 36.0 and 18.7%, indicates that the kerogen concentrates account for over 80% of the TOC in the shales. XRD shows clay mineral content of SH1 (18.4%) is much lower than SH2 (35.8%), while the quartz content of 55.4% for SH1 is higher than that of 41.7% for SH2.

For the 95% R.H. moisture equilibrated samples, the kerogen concentrates adsorb much more water (15.5 and 13.0 wt.%) than the shales (1.48 and 1.22 wt.%), due to their higher SA and pore volumes. The high moisture contents of the kerogens could in part arise from demineralisation opening inaccessible pores in the shales.

3.2 Pore structure from FE-SEM

FE-SEM can observe pores larger than 100 nm in shales (Loucks et al., 2012; Loucks et al., 2009; Milliken et al., 2013; Zou et al., 2010) and Figure 1 shows that the region of most organic matter is in the range of 5-20 µm, surrounded by minerals (Figure 1A) and a large number of macropores in the organic matter (Figure 1A). Intra-particle macropores in the organic matter are evident (Figure 1B, C) with irregular shapes (Figure 1B), with only a few pores larger than 500 nm (Figure 1D). The most minerals contain inter-particle pores (Figure 1C).

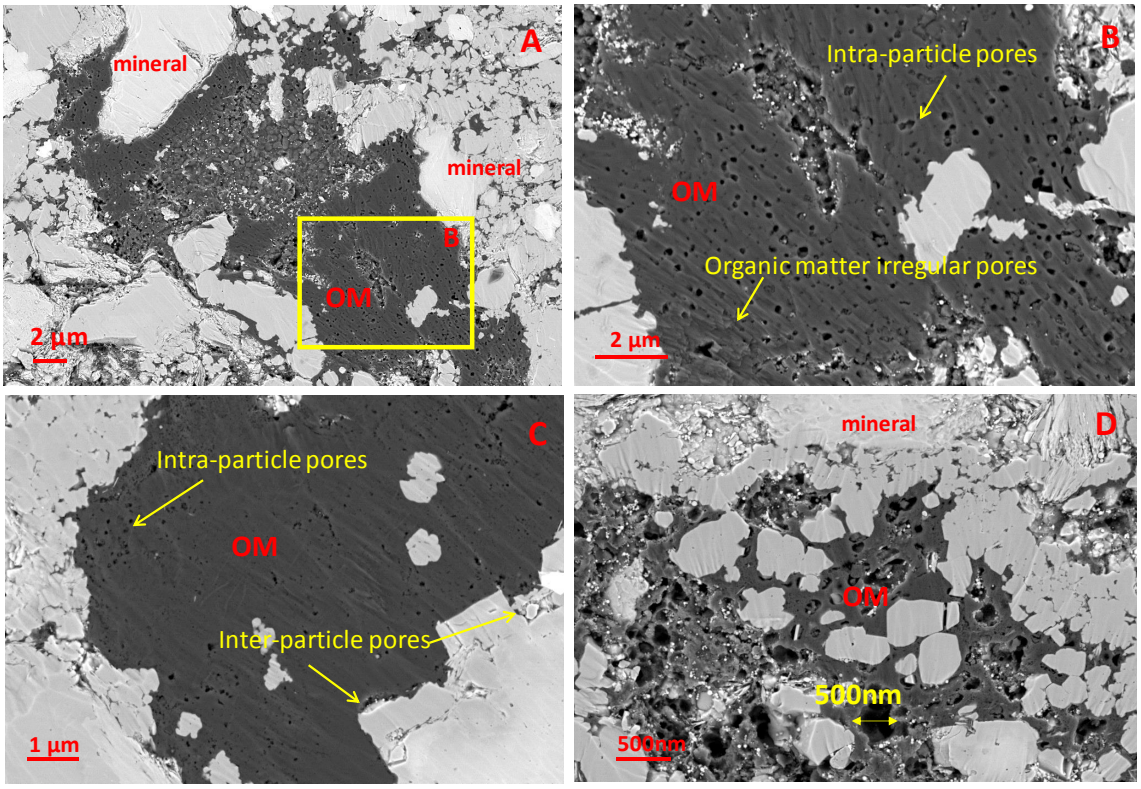

Figure 1. FE-SEM images of organic matter and macropores in shales. A) Minerals and organic matter (OM) distribution in SH2, B) is the enlarged figure of A, OM irregular pores in SH2, C) Intra-particle pores and inter-particle pores in SH1, D) The size of OM pores in SH2.

3.3 Methane adsorption capacities of the shales and kerogen concentrates

3.3.1 Moisture impact on methane adsorption capacity Figure 2 indicates that the dry kerogen concentrates and shales have much higher methane adsorption capacities than their wet counterparts. Approximately 72 and 54% of the equilibrium methane adsorption capacities are lost for K1 and K2, respectively (K1 reducing from 22.2 mg/g to 6.2 mg/g, and K2 from 12.5 mg/g to 5.8 mg/g, Table 2). The same pattern is found for the shale samples, with approximately 50% of equilibrium methane capacities of the dry shales being lost (SH1 reducing from 2.7 mg/g to 1.5 mg/g, and SH2 from 2.0 mg/g to 0.98 mg/g wet, Table 2). The level of reduction for the shales is consistent with previous studies (Gasparik et al., 2014; Merkel et al., 2016; Whitelaw et al., 2019). A significant decrease in adsorption capacity of 40-60% was observed between the dry and moisture equilibrated shale samples studied by Gasparik et al. (2014). Merkel et al. (2016) found that Lacustrine shales lose 20-80% of initial dry adsorption capacity upon full moisture equilibration (97% R.H.). Whitelaw et al. (2019) also found that equilibrated methane adsorption amount dropped by 27% after the shale samples were equilibrated at 50% R.H..

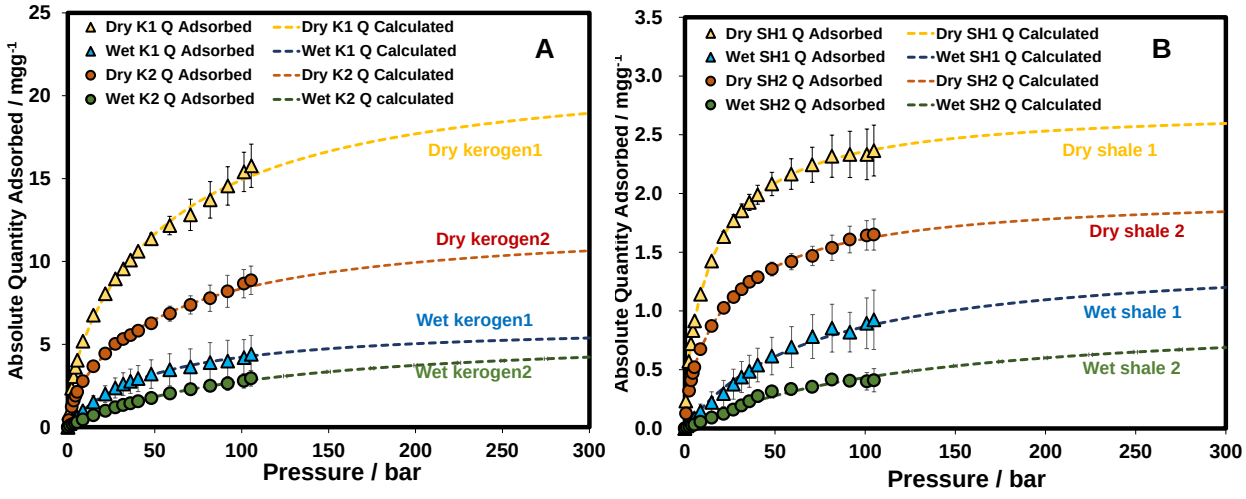

Figure 2. Comparison of absolute methane adsorption isotherms of dry and wet (95% R.H.) kerogen concentrates and shales at 25 °C. A) dry and wet kerogen concentrates, B) dry and wet shales. Each sample was analysed in triplicate by HPVA, the data points are the mean from triplicate experiments and the error bars represent the dispersion of a dataset relative to its mean.

The dry shales have slightly steeper isotherms (Type 1a) than their kerogen counterparts (Type 1b) and for the wet shales, the isotherm shapes are quite similar to those wet kerogens

(Figure 2), which are being less steep than the dry kerogens. This suggests, for the shales, that moisture preferentially reduces access to the smaller micropores, as intuitively expected. The shallower isotherms for the dry kerogen concentrates compared to the dry shales suggests that isolated kerogens have higher proportion of larger micropores and smaller mesopores, which are accessed by demineralisation. K1 suffers a greater proportional loss in methane adsorption than K2 due to K1 containing the greater proportion of micropores as discussed in section 3.4.

3.3.2 Contribution of kerogen concentrates to the methane adsorption capacities of the shales The methane adsorption capacities for the kerogen concentrates and corresponding shales are compared in Table 2, which lists the contributions of the kerogen concentrates made to methane adsorption capacities for the shales under dry and wet conditions. The contributions from the kerogen concentrates to the methane adsorption capacities are calculated from the yields of kerogen concentrates from shales using equation (7), and these are expressed as a percentage using equation (8).

$$Q_{contribution} = Y_K \times Q_K \quad (7)$$

$$R_K = 100\% \times (Q_{contribution}/Q_{SH}) \quad (8)$$

Where, $Q_{contribution}$ is the quantity of methane adsorbed by the kerogen concentrates per gram shale; Y_K is the yield of kerogen concentrate; Q_K is the methane adsorption quantity of the kerogen concentrate; R_K is the percentage that the kerogen concentrate contributes to the methane adsorption in shale; Q_{SH} is the methane adsorption quantity of shale.

As expected, Table 2 indicates that kerogen concentrates have greater methane adsorption capacities than shales, both under dry and wet conditions. For the dry samples, the equilibrium adsorbed methane quantity for K1 is 22.2 mg/g, which is about 8 times higher than that for the SH1 (2.7 mg/g). The equilibrium adsorbed methane quantity of K2 (12.5 mg/g) is more than 6 times higher than that of SH2 (2.0 mg/g). K1 and K2 account for 97 and 68% of the equilibrium methane uptakes for the dry shales, respectively. These contributions are higher than those of about 50% reported in other studies (Fan et al., 2014; Rexer et al., 2014) probably because the kerogens in this research are from overmatured shales, which are likely to contain more pores for methane adsorption. Due to the different isotherm profiles, at low pressure (5 bar), the dry kerogen concentrates nominally account for much

less of the methane adsorption for the dry shales, 53 and 45% for SH1 and SH2, respectively. The ratio of the kerogen concentrate contribution increases with pressure. Most of methane adsorption of the dry shales takes place at a relatively low-pressure range due to the higher proportion of small micropores (Table 3). Moreover, dry kerogens, as discussed earlier (section 3.3.1), with larger micropores and small mesopores could have higher methane adsorption capacities than the organic matter in shales.

Table 2. Methane adsorption capacities of the kerogen concentrates and shales, and the contributions made by kerogen concentrates to the capacities of the shales.

	Dry sample 1				Dry sample 2			
Pressure (bar)	Q_{K1} (mg/g)	Q_{SH1} (mg/g)	K1-$Q_{contribution}$ (mg/g)	R_{K1} (%)	Q_{K2} (mg/g)	Q_{SH2} (mg/g)	K2-$Q_{contribution}$ (mg/g)	R_{K2} (%)
5	4.0±0.1	0.9±0.1	0.5±0.1	53±1	2.1±0.1	0.5±0.1	0.2±0.1	45±1
50	11.5±0.3	2.1±0.1	1.4±0.1	66±4	6.3±0.3	1.4±0.1	0.7±0.1	50±4
100	15.4±1.2	2.3±0.2	1.9±0.1	79±10	8.7±0.9	1.6±0.1	1.0±0.1	58±7
150	16.6±1.4	2.5±0.2	2.0±0.2	81±10	9.3±0.9	1.7±0.1	1.0±0.1	59±7
300	18.9±1.6	2.6±0.2	2.3±0.2	88±11	10.6±1.0	1.9±0.2	1.2±0.1	63±8
Qm	22.2±1.8	2.7±0.3	2.7±0.2	97±12	12.5±1.2	2.0±0.2	1.4±0.1	68±9
	Wet sample 1				Wet sample 2			
Pressure (bar)	Q_{K1} (mg/g)	Q_{SH1} (mg/g)	K1-$Q_{contribution}$ (mg/g)	R_{K1} (%)	Q_{K2} (mg/g)	Q_{SH2} (mg/g)	K2-$Q_{contribution}$ (mg/g)	R_{K2} (%)
5	0.6±0.2	0.1±0.1	0.08±0.02	86±24	0.3±0.1	0.03±0.01	0.03±0.01	99±11
50	3.2±0.9	0.6±0.2	0.39±0.10	63±23	1.8±0.2	0.33±0.04	0.19±0.02	61±9
100	4.2±1.1	0.9±0.2	0.50±0.13	56±20	2.8±0.4	0.40±0.07	0.31±0.05	76±18
150	4.7±1.2	1.0±0.3	0.57±0.15	57±21	3.3±0.5	0.53±0.13	0.36±0.06	69±20
300	5.4±1.4	1.2±0.3	0.65±0.17	54±20	4.2±0.7	0.69±0.17	0.46±0.07	67±19
Qm	6.2±1.6	1.5±0.4	0.75±0.19	50±18	5.8±0.9	0.98±0.24	0.63±0.10	64±18

Q is the absolute methane quantity adsorbed by kerogen concentrate and shale from HPVA, $Q_{contribution}$ is the methane amount adsorbed by kerogen per gram of shale, calculated based on equation (7). R is the percentage kerogen concentrate contribution to the methane adsorption capacity of the shale calculated by equation (8). Q after pressure 105 bar is predicted by the Dual-site Langmuir model. Q_m is the predicted maximum methane amount adsorbed (monolayer capacity) when the isotherm reach equilibrium. The data points are the mean from triplicate experiments and the errors represent the dispersion of a dataset relative to its mean.

For the wet samples, the methane adsorption capacities of the kerogen concentrates are about 4-6 times higher than corresponding shales. K1 and K2 account for 50 and 64% respectively, of the methane adsorbed in the wet shales. However, in contrast to the dry samples, the apparent contributions of the kerogen concentrates to methane adsorption capacities of the shales decrease with increasing pressure. Although moisture reduces the accessible micropores for methane adsorption for both shales and kerogen concentrates and results in shallower isotherms (Figure 2), the micropores in kerogen concentrates dominate methane adsorption in wet shales at low pressure (5 bar) with contribution ratios for K1 and K2 are 86 and 99% respectively, indicating minimal adsorption on minerals (Li et al., 2016; Li et al., 2019).

3.4 Pore characterization of the shales and kerogen concentrates

3.4.1 Moisture impact on low-pressure gas sorption isotherms The low-pressure gas (N_2, CO_2) isotherms of the dry and wet kerogen concentrates and shales are compared in Figure 3 and 4. The CO_2 adsorption isotherms (Figure 4) are type I(b) and the N_2 sorption isotherms are type IV(a) with a hysteresis loop (Figure 3), a steeper gas uptake at low relative pressure arises from a higher proportion narrow micropores (Thommes et al., 2015). This confirms that the shales and kerogen concentrates contain mesopores and macropores, with the N_2 isotherms showing adsorption at a low relative pressure ($P/P°<0.1$) from micropores. The CO_2 isotherms show adsorption solely associated with micropores for both the shales and kerogen concentrates.

The quantity of adsorbed N_2 and shape of the hysteresis patterns of the dry and wet shales and kerogen concentrates are slightly different. For the dry shales (Figure 3A), the hysteresis loop is similar to hysteresis type H2 based on the classification of the hysteresis (Sing, 1985) which suggests the pores are very complex, with pore shapes including ink-bottle pores comprising necks and windows, inhomogeneous cylinder, slit and sphere pores, and other irregular pores (Sing, 1985; Thommes et al., 2015). The obvious desorption plateau in H2 hysteresis means there is pore-blocking or shielding from a narrow range of pore necks/windows, as cavitation occurs between 0.4-0.5 P/P°, indicating these necks and windows are all approximately <4 nm. This phenomenon still exists for wet shales (Figure 3B) having same isotherm and hysteresis types, but at a reduced pore volume or quantity of

adsorbed N_2, indicating water is blocking a large majority of the pore and neck/window volume.

For the dry kerogen concentrates (Figure 3C), the hysteresis loop is very similar to type H3 (Sing, 1985; Thommes et al., 2015), and adsorption occurs at low-pressure, this indicates most of the pores are micro and mesopores with slit shape pore geometry. Pore necks/windows exist in kerogen concentrates with a large range between 4-100 nm, as well as a smaller necks/windows <4 nm. However, most of these neck and window pores are blocked or filled when kerogen concentrates are equilibrated with moisture at 95% R.H. reducing interconnectivity (shown in Figure 3D, with little or no hysteresis for K1 and K2), and reducing N_2 adsorption.

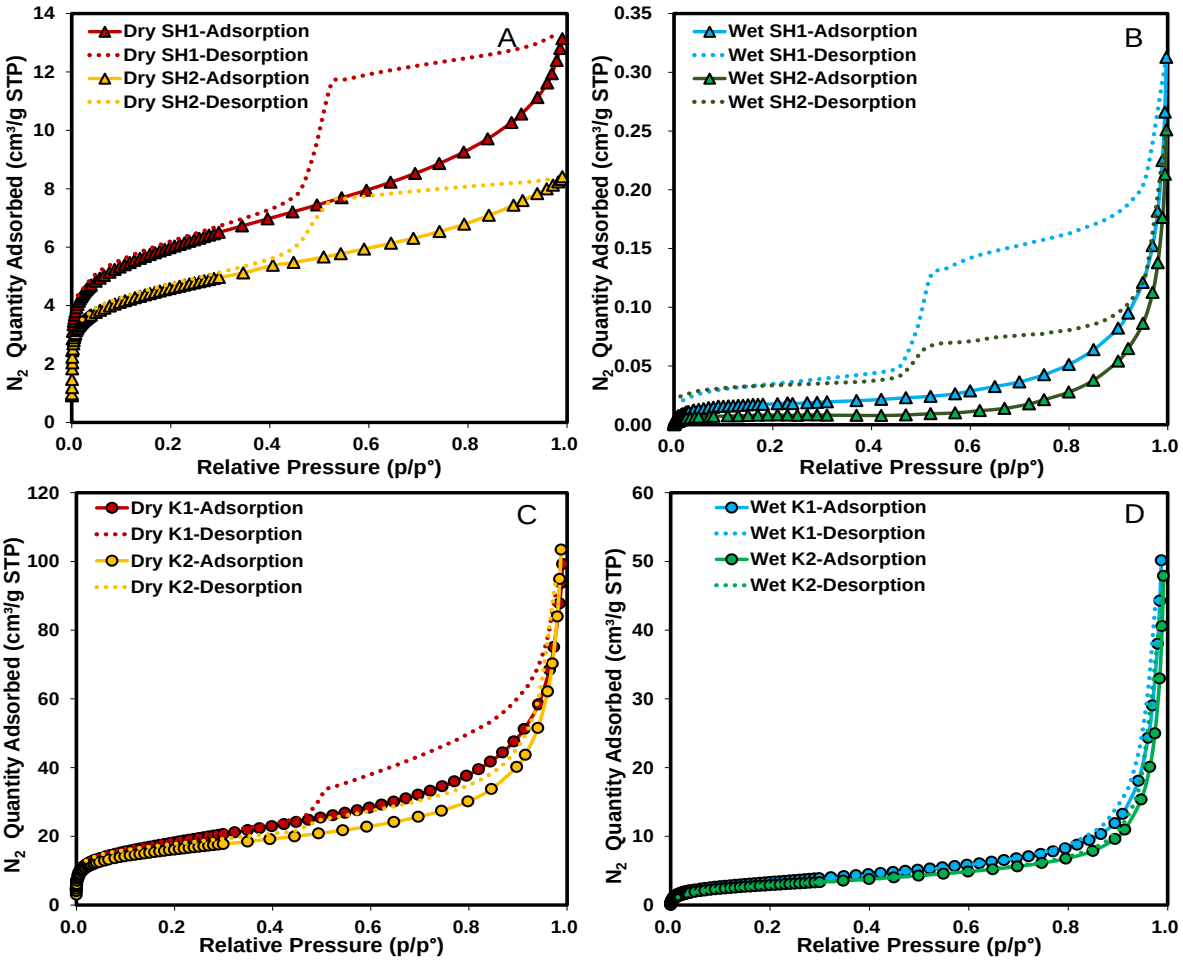

Figure 3. A comparison of low-pressure N_2 sorption isotherms of shales and kerogen concentrates under wet and dry conditions. A) N_2 isotherms of dry shales, B) N_2 isotherms of wet shales, C) N_2 isotherms of dry kerogen concentrates, D) N_2 isotherms of wet kerogen

concentrates. P/P°, relative pressure, P is the absolute equilibrium pressure and P° is the saturation pressure of N_2 at -196 °C, 1 bar.

As expected, the extents of N_2 and CO_2 adsorption are much greater for the kerogen concentrates than the corresponding shales. Table 3 indicates that the maximum amounts of adsorbed N_2 for the dry kerogen concentrates are 99.2 and 103.4 cm^3/g which are 7-12 times higher than the corresponding dry shales (13.3 and 8.4 cm^3/g, respectively). SH1 and K1 have the higher SA and pore volume than SH2 and K2 as they have the higher TOC (Table 1). Similar differences are observed for CO_2 adsorption (Figure 4), the maximum adsorbed CO_2 quantities are 10.9 and 8.9 cm^3/g on the two dry kerogen concentrates, which are about 4-5 times higher than the dry shales (2.4 and 1.7 cm^3/g) (Table 3). The BET SAs estimated from the N_2 isotherms are quite close to those from the CO_2 isotherms of the dry samples (Table 3), indicating the N_2 penetrates all the micropores that CO_2 can. Figure 4 indicates for the dry kerogens that K1 contains a greater micropore surface area (Table 3) and a greater proportion of smaller micropores than K2, consistent with the steeper methane adsorption isotherms (Figure 2).

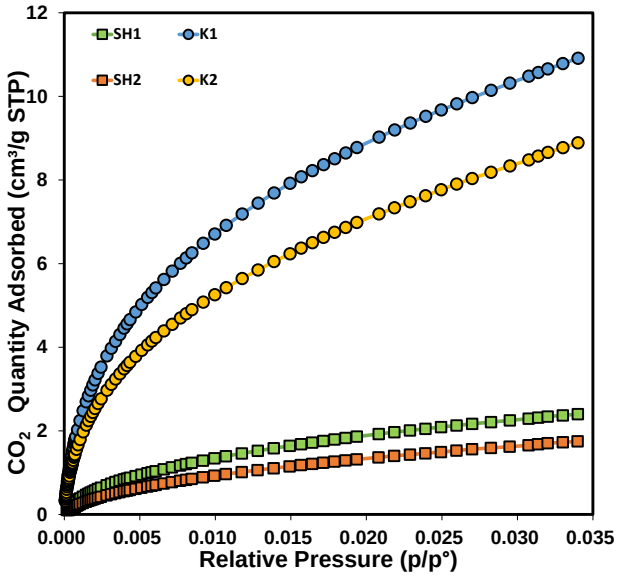

Figure 4. Comparison of low-pressure CO_2 adsorption isotherms of dry kerogen concentrates and shales at 0 °C. P/P°, relative pressure, P is the absolute equilibrium pressure and P° is the saturation pressure of CO_2 at 0 °C, 34.9 bar.

3.4.2 Moisture impact on pore characteristics Table 3 reveals that more than 81% of the BET SA for the kerogen concentrates is lost, at 95% R.H., K1 and K2, reducing from 65.7-58.8 m^2/g to 12.4-10.8 m^2/g, and 48-59% total pore volume is lost, reducing from 0.14-0.15 cm^3/g to

0.073-0.062 cm³/g. The impact of moisture on the shales is even greater, with over 99% reduction in BET SA for SH1 and SH2, reducing from 21.7-16.7 m^2/g to 0.075-0.029 m^2/g, respectively, accompanied by a 98% loss in total pore volume.

Table 3. Maximum adsorbed gas quantities, surface areas and pore volumes of the shales and kerogen concentrates.

Sample	N_2 $Q_{Adsorbed}$ (cm^3/g)	CO_2 $Q_{Adsorbed}$ (cm^3/g)	SA_{BET} (m^2/g)	CO_2 SA_{BET} (m^2/g)	V_{micro} (cm^3/g)	V_{meso} (cm^3/g)	V_{macro} (cm^3/g)	V_{total} (cm^3/g)
Dry K1	99.2	10.9	65.7	68.0	0.0141	0.110	0.018	0.14
Dry K2	103.4	8.9	58.8	57.9	0.0140	0.114	0.023	0.15
Wet K1	50.1	/	12.4	/	0.0010	0.058	0.014	0.073
Wet K2	47.9	/	10.8	/	0.0011	0.044	0.017	0.062
Reduction K1 (%)	49	/	81	/	93	47	20	48
Reduction K2 (%)	54	/	82	/	92	62	24	59
Dry SH1	13.1	2.4	21.7	16.1	0.0069	0.012	0.00075	0.019
Dry SH2	8.4	1.7	16.7	12.6	0.0054	0.0067	0.00016	0.012
Wet SH1	0.31	/	0.075	/	0.0000039	0.00028	0.000063	0.00034
Wet SH2	0.25	/	0.029	/	0	0.00021	0.000056	0.00027
Reduction SH1 (%)	98	/	99.7	/	99.9	98	92	98
Reduction SH2 (%)	97	/	99.8	/	100	97	66	98

N_2 $Q_{Adsorbed}$ is the maximum adsorbed at 0.995 P/P°; CO_2 $Q_{Adsorbed}$ is the maximum adsorbed at 3.5×10^{-2} P/P°; SA_{BET} and CO_2 SA_{BET} are the surface areas calculated by BET theory; V_{micro}, V_{meso}, V_{macro} and V_{total} are the micropores, mesopore, macropore and the total pore volume (up to 100 nm) calculated by the NLDFT model.

Moisture also changes the PSD for the kerogen concentrates and shales, the cumulative SA rises rapidly in the micropore range (Figure 5A, 5C), and the micropores and small mesopores (less than 10 nm) contribute most of the SA (Figure 5B, 5D). Whereas for the wet kerogen concentrates and shales, micropores only make a small contribution to SA (Figure 5E, 5G). Micropores less than 1.3 nm provide virtually zero SA, making mesopores dominant for the wet samples (Figure 5F, 5H), suggesting pores less than 1.3 nm are either blocked or filled with water. Micropores contribute 9 and 10% for K1 and K2 and 36 and 44% for SH1 and SH2, respectively, of the pore volume (Figure 6A, 6C), consistent with the steeper methane adsorption isotherms observed for the shales (Figure 2). However, micropores contribute only less than 2% for the wet samples (Figure 6E, 6G), indicating most micropores especially micropores less than 1.3 nm are blocked by water. This can also reduce the interconnectivity

to larger pores reducing the pore volume in meso and macropores, but by a lesser extent (Table 3). Although mesopores contribute more than 55% of the total pore volume for both the dry or wet samples, the dry kerogen concentrates and shales have larger proportions of the volume as small mesopores (pore less than 10 nm) (Figure 6B, 6D) and these make the largest contribution to the total pore volume, while for wet kerogen concentrates and shales, the mesopores larger than 10 nm have a greater contribution (Figure 6F, 6H).

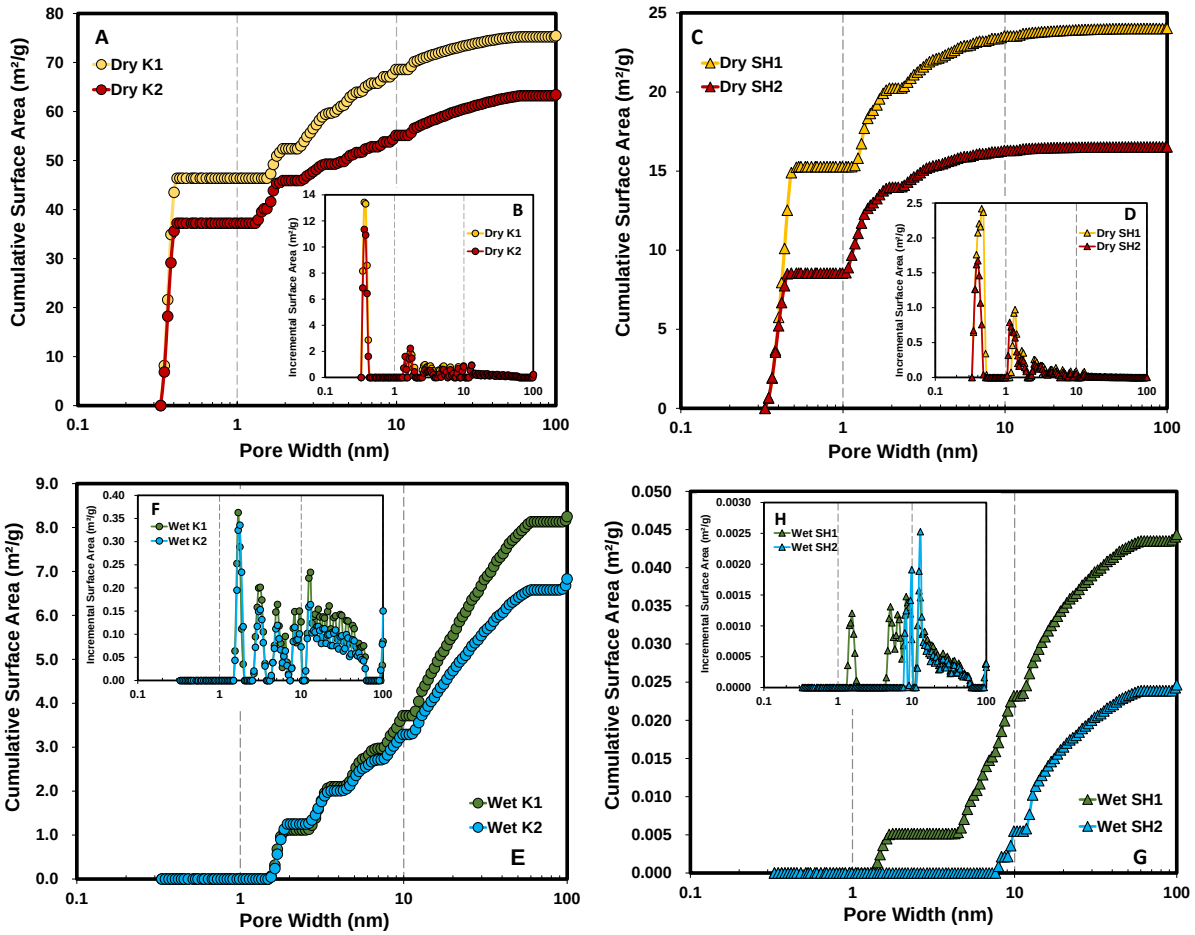

Figure 5. PSD and SA of dry (by N_2 and CO_2) and wet (by N_2) kerogen concentrates and shales. A) Cumulative SA and the pore width of dry kerogen concentrates, B) Incremental SA and pore width of dry kerogen concentrates, C) Cumulative SA and the pore width of dry shales, D) Incremental SA and pore width of dry shales, E) Cumulative SA and the pore width of wet kerogen concentrates, F) Incremental SA and pore width of wet kerogen concentrates, G) Cumulative SA and the pore width of wet shales, H) Incremental SA and pore width of wet shales.

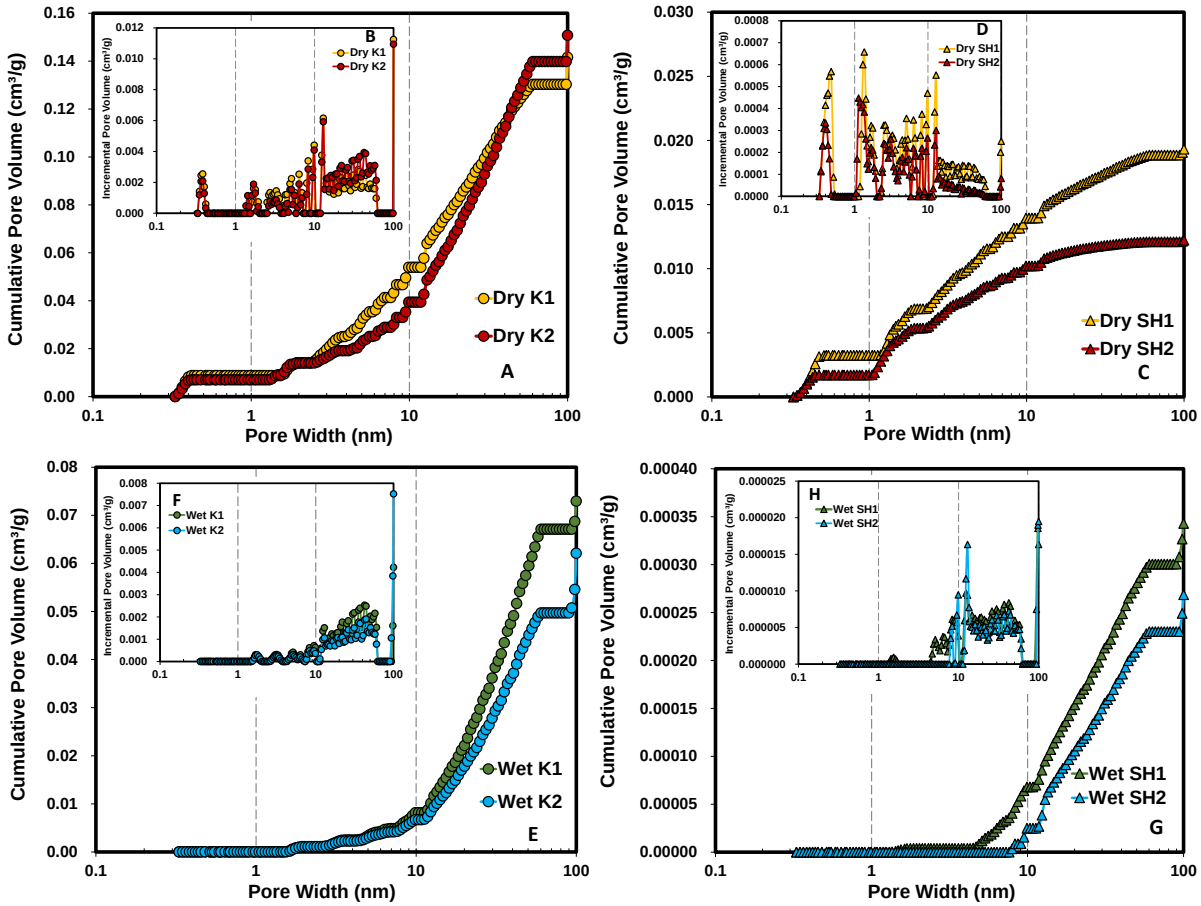

Figure 6. PSD and pore volume of dry (by N_2 and CO_2) and wet (by N_2) kerogen concentrates and shales. A) Cumulative pore volume and the pore width of dry kerogen concentrates, B) Incremental pore volume and pore width of dry kerogen concentrates, C) Cumulative pore volume and the pore width of dry shales, D) Incremental pore volume and pore width of dry shales, E) Cumulative pore volume and the pore width of wet kerogen concentrates, F) Incremental pore volume and pore width of wet kerogen concentrates, G) Cumulative pore volume and the pore width of wet shales, H) Incremental pore volume and pore width of wet shales.

Table 3 confirms that moisture has the greatest impact on micropores, followed by mesopores and macropores in both kerogen concentrates (93-92, 47-62 and 20-24% reductions for micropore, mesopore, and macropore volumes, respectively) and shales (99.9-100, 98-97 and 92-66%, respectively), which makes the extent of reduction for SA larger than that for pore volume since most of the SA is provided by micropores, whereas most of the pore volume is provided by mesopores. Also, Table 3 indicates that the reduction in SA and pore volume for the shales are much higher than for the kerogen concentrates. This is because

the proportion of micropores in shale (36-44%) is much higher than for kerogen (9-10%). In addition, the large amount of clay minerals in some shales are responsible for these shales being most easily affected by water (Feng et al., 2018; Ismadji et al., 2015; Kuila et al., 2014; Liming et al., 2012b; Zhu and Xia, 2013).

Water molecules hinder access to the smaller micropores, as shown in Figure 5 and 6, for a cylindrical/slit pore with a diameter of equal to or less than 1.3 nm. Less water is adsorbed in the larger micropores (together with mesopores) due to the reducing energy potential for adsorption (Dubinin, 1966; Gregg and Sing, 1982; Ruthven, 1984). Also, water is adsorbed in micropores first when these can be accessed. For the pores larger than 1.3 nm, water occupies some adsorption sites and can form a cluster of molecules leading to a film (or condensate) which reduces both the accessible pore volume and SA, while other gases can still gain access if the pores are not totally blocked. It is believed that thicker water films can reduce pore volume more (Li et al., 2016). The low-pressure adsorption isotherm results have indicated that the micropores, mesopores and macropores are largely connected by narrow pore necks building a complex pore system. The water volume uptake calculated by equation (2) indicates that 33 and 40% of the pore volume for SH1 and SH2 are occupied by water, whereas more than 98% accessible pore volume of shales are reduced after sample become wet, suggesting the water reduce the pore volume by taking up the pore volume as well as by blocking the micropore pore necks connecting to larger pores. The size of the pore neck matters, when the pore necks are less than 1.3 nm, water molecule clusters can block the necks preventing other gases being transported into larger pores, but when the pore neck is larger, there is still enough space for the other gas to go into the bigger pores.

3.5 Depiction of the impact of moisture on methane adsorption capacity

Figure 7 illustrates how moisture can reduce the methane adsorption capacity for kerogens by 1) occupying adsorption surfaces. Water, as the polar molecule gives stronger interactions with the same adsorption surface (non-polar or polar) than the non-polar methane molecules, can occupy adsorption sites (Chalmers and Bustin, 2010; Chalmers and Bustin, 2007); 2) blocking micropore access and filing mesopores. As for the mesopores connecting with different size of pore necks (smaller than 1.3 nm and larger than 1.3 nm) methane can occupy most of the sorption surface in the dry samples (Figure 7A). However, after samples become wet, much of the available sorption surface is taken up by water, or most pores with narrow

pore necks become inaccessible since water blocks access to micropore less than 1.3 nm (Figure 7B).

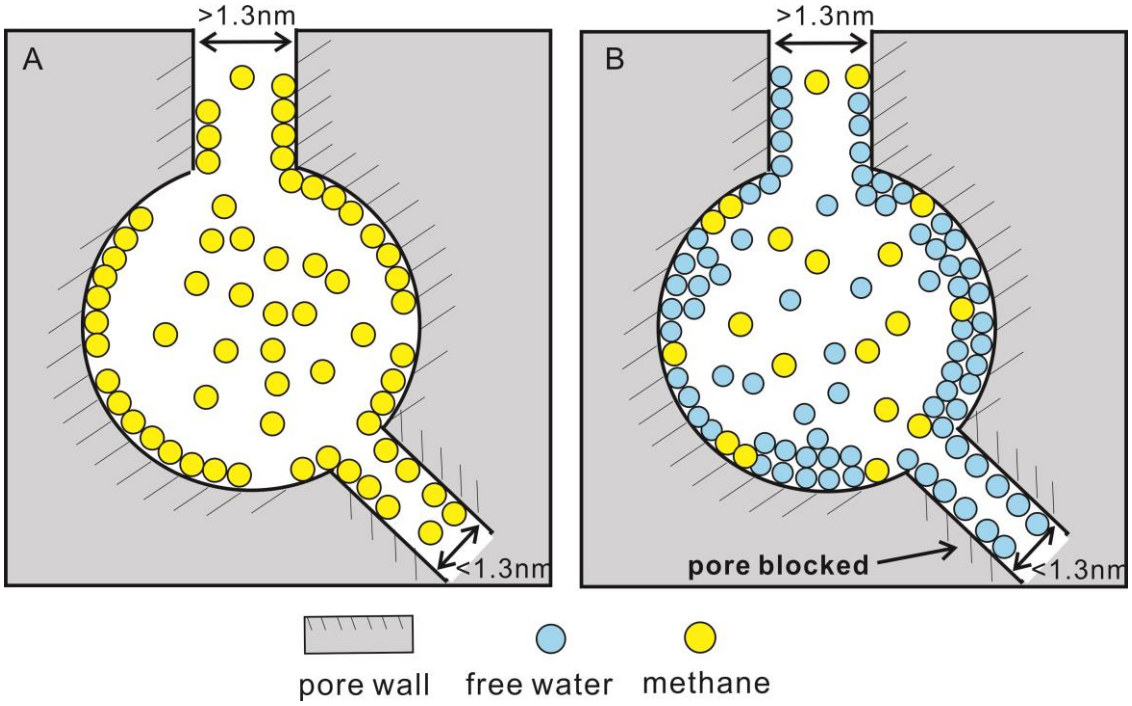

Figure 7. Moisture impact on methane adsorption in small mesopore and connecting micropores for kerogens. A) Methane adsorption in dry samples, B) Methane adsorption in wet samples, with water blocking micropore access and filling mesopores.

Moisture can affect methane adsorption differently for kerogen concentrates and shales. According to methane adsorption results, the reduction of K1 (72%) is higher than K2 (54%) since K1 has more narrow pore necks as more evident cavitation occurs in the desorption isotherms (Figure 3C), and most pore necks are blocked after moisture equilibrated (Figure 3D with little or no hysteresis). However, for shales, the reductions (46-51%) are comparable as they have similar pore networks (Figure 3A). Furthermore, the reductions in SA and pore volume measured are higher than those for the equilibrium methane adsorption capacities. This can be explained by ice having a greater effect on blocking access to pores than water. It is because the SA and pore volume are measured at sorption experiment temperature of -196 °C for low-pressure N_2, bulk pore water or water clusters will exist as ice crystals (Pauling, 1935), with a lattice of 0.45 nm width and 0.73 nm height (Bragg, 1921), which could occupy more space so reducing pore SA and volume to a greater extent. Whereas water molecules are depicted with a diameter of 0.28 nm (D'Arrigo, 1978; Zhang and Xu, 1995) in the methane

adsorption experiment temperature (25 °C). Furthermore, the pore blocking threshold of 1.3 nm occurs with ice crystals but not necessarily water meaning the blocking effects are probably slightly exaggerated at -196 °C.

4. Implication for GIP

The classical GIP is estimated from the total amount of free gas and adsorbed gas content by equation (9) (Tang et al., 2016). However, most GIP estimations use dry samples without considering the effect of moisture, and therefore could be overestimated. This research provides a realistic method for the measurement of the accessible pore volume of moisture equilibrated shales and reveal the moisture impact on the adsorbed gas content, making a more accurate GIP estimation of wet shales possible. The GIPs of dry and wet shales are listed in Table 4 which are calculated by equation (9), the dry porosity is obtained from MIP and wet porosity is calculated based on equation (10).

$$GIP = n_{free} + n_a = n_{free} + n_e + V_a \times \rho_g = V_{tot} \times \rho_g + n_e \quad (9)$$

$$Porosity_{wet} = \frac{V_{wet\ pore}}{V_{sh}} = 1 - \frac{\rho_{wet\ bulk}}{\rho_{wet\ sk}} = 1 - \frac{\rho_{dry\ bulk}}{\rho_{wet\ sk}} \times (1 + W) \quad (10)$$

where, n_{free} is the free gas in the pore; n_a is the absolute adsorption quantity; n_e is the excess adsorption quantity; V_a is the pore volume for gas to adsorb into; ρ_g is the density of the bulk gas; V_{tot} is the total pore volume accessible to gas in shale; $Porosity_{wet}$ is the porosity of wet shale; $V_{wet\ pore}$ is the pore volume of wet shale; V_{sh} is the shale sample volume.

Table 4. The porosity, total pore volume and the estimated GIP of shales.

Sample	Porosity (%)	V_{tot} (m^3/t)	n_a (kg/t)	n_{free} (kg/t)	GIP (kg/t)
Dry SH1	10.2	0.043	1.5	10.4	11.9
Dry SH2	4.0	0.016	1.1	3.7	4.8
Wet SH1	6.8	0.028	0.73	6.9	7.6
Wet SH2	2.4	0.009	0.44	2.2	2.7

Pressure and temperature effects on the free and adsorbed gas content cannot be neglected (Chen et al., 2018; Luffel and Guidry, 1992; Ross and Bustin, 2007; Tang et al., 2016). It is estimated that the actual shale reservoir pressure and temperature of Longmaxi shale,

Sichuan Basin with a depth of 4000 m are about 600 bar and more than 100 °C (Li et al., 2018; Tang et al., 2016). An average reduction of 45% for adsorbed gas content from 25 °C to 100 °C is applied based on the literature (Ji et al., 2015; Rexer et al., 2013; Whitelaw et al., 2019; Zou et al., 2017). The total accessible pore volume (V_{tot}) of shale is calculated from the porosity, the density of methane at 600 bar and 100 °C is 241.03 kg/m^3 obtained from REFPROP version 8.0 software and the excess adsorption quantity (equation (3)) is from the methane adsorption experiments. The estimated GIP of the shales at 600 bar and 100 °C are listed in Table 4, and the dominant gas is free gas for both dry and wet shales. The calculated GIP of the dry shales, SH1 and SH2 (maximum GIP) are 11.9 and 4.8 kg/t, respectively, similar to the range of 3.2-6.4 kg/t for Longmaxi shale (Tang et al., 2016). The GIP of the wet shales Sha and SH2 (minimum GIP) are 7.6 and 2.7 kg/t, respectively, indicating that the estimated GIP can reduce by up to 36-45% when moisture is considered.

5. Conclusions

This is the first time that the impact of moisture on PSD and methane adsorption capacities of kerogens and shales have been compared and the following conclusions can be drawn.

(1) Moisture has a detrimental effect on methane adsorption capacity, reductions for the kerogen concentrates and shales being 54-72% and 46-51%, respectively, at 95% R.H.. The kerogen concentrates account for most (97 and 68% for dry SH1 and SH2, 50 and 64% for wet SH1 and SH2) of the equilibrium methane adsorption capacities of the shales within experimental error.

(2) Dry shales display a steeper rise of methane adsorption at lower pressures than dry kerogen concentrates. Although dry shales have lower pore volume than dry kerogen, it is likely that the higher proportion of micropores in the dry shales investigated account for equilibrium being reached at low pressure ranges.

(3) The kerogen concentrates have much higher average SA (62.2 m^2/g compared to 19.2 m^2/g) and average pore volume (0.15 cm^3/g compared to 0.016 cm^3/g) than corresponding shales. Moisture significantly reduces the SA (81% for kerogen, and 99% for shale) and total pore volume for kerogens concentrates (48-49%) and shales (98%). Micropore and narrow mesopores (<10 nm) are dominant for dry samples, whereas at 95% R.H. micropores less than 1.3 nm are filled or blocked by moisture obstructing pore necks and windows connecting to micropores and mesopores stopping gas transport. These

reductions are much larger than reductions observed for methane adsorption as ice in the N_2 low-pressure measurements reducing access to pores much more than liquid water for methane adsorption.

(4) This research provides a realistic method for accurate GIP estimation of moisture equilibrated shales. The calculated GIP of the dry SH1 and SH2 (maximum GIP) are 11.9 and 4.8 kg/t, and the GIP of the wet shales (minimum GIP) 7.6 and 2.7 kg/t, indicating the GIP reduces by 36-45% when moisture is considered for the shales investigated.

Acknowledgments

The authors greatly acknowledge financial support by the National Environment Research Council (Grant no: NE/C507002/1) and the Faculty of Engineering Research Excellence PhD Scholarship for Wei Li provided by the University of Nottingham. The British Geological Survey is acknowledged for experimental support.

References

Abràmoff, M.D., Magalhães, P.J., Ram, S.J., 2004. Image processing with ImageJ. Biophotonics international 11, 36-42.

Adesida, A.G., Akkutlu, I., Resasco, D.E., Rai, C.S., 2011. Characterization of barnett shale kerogen pore size distribution using DFT analysis and grand canonical monte carlo simulations, SPE annual technical conference and exhibition. Society of Petroleum Engineers.

Bragg, W., 1921. The crystal structure of ice. Proceedings of the Physical Society of London 34, 98.

Brunauer, S., Emmett, P.H., Teller, E., 1938. Adsorption of gases in multimolecular layers. Journal of the American chemical society 60, 309-319.

Cao, T., Song, Z., Wang, S., Xia, J., 2015. A comparative study of the specific surface area and pore structure of different shales and their kerogens. Science China Earth Sciences 58, 510-522.

Chalmers, G.R., Bustin, M.R., 2010. PS The Effects and Distribution of Moisture in Gas Shale Reservoir Systems. AAPG Annual Convention and Exhibition.

Chalmers, G.R., Bustin, R.M., 2007. The organic matter distribution and methane capacity of the Lower Cretaceous strata of Northeastern British Columbia, Canada. International Journal of Coal Geology 70, 223-239.

Chen, C., Hu, D., Westacott, D., Loveless, D., 2013. Nanometer - scale characterization of microscopic pores in shale kerogen by image analysis and pore - scale modeling. Geochemistry, Geophysics, Geosystems 14, 4066-4075.

Chen, M., Kang, Y., Zhang, T., Li, X., Wu, K., Chen, Z., 2018. Methane adsorption behavior on shale matrix at in-situ pressure and temperature conditions: Measurement and modeling. Fuel 228, 39-49.

Chen, Y., Jiang, S., Zhang, D., Liu, C., 2017. An adsorbed gas estimation model for shale gas reservoirs via statistical learning. Applied energy 197, 327-341.

Curtis, J.B., 2002. Fractured shale-gas systems. AAPG bulletin 86, 1921-1938.

D'Arrigo, J.S., 1978. Screening of membrane surface charges by divalent cations: an atomic representation. American Journal of Physiology-Cell Physiology 235, C109-C117.

Day, S., Sakurovs, R., Weir, S., 2008. Supercritical gas sorption on moist coals. International Journal of Coal Geology 74, 203-214.

Dong, D., Shi, Z., Guan, Q., Jiang, S., Zhang, M., Zhang, C., Wang, S., Sun, S., Yu, R., Liu, D., 2018. Progress, challenges and prospects of shale gas exploration in the Wufeng–Longmaxi reservoirs in the Sichuan Basin. Natural Gas Industry B 5, 415-424.
Dongjun, F., Zongquan, H., Bo, G., Yongmin, P., Wei, D., 2016. Analysis of shale gas reservoir—forming condition of Wufeng Formation—Longmaxi Formation in Southeast Sichuan Basin. Geological Review 62, 1521-1532.
Dubinin, M., 1966. Chemistry and physics of carbon. M. Dekker, New York, 51-120.
Durand, B., 1980. Kerogen: Insoluble organic matter from sedimentary rocks. Editions technip.
Fan, E., Tang, S., Zhang, C., Guo, Q., Sun, C., 2014. Methane sorption capacity of organics and clays in high-over matured shale-gas systems. Energy Exploration and Exploitation 32, 927-942.
Feng, D., Li, X., Wang, X., Li, J., Sun, F., Sun, Z., Zhang, T., Li, P., Chen, Y., Zhang, X., 2018. Water adsorption and its impact on the pore structure characteristics of shale clay. Applied Clay Science 155, 126-138.
Gasparik, M., Bertier, P., Gensterblum, Y., Ghanizadeh, A., Krooss, B.M., Littke, R., 2014. Geological controls on the methane storage capacity in organic-rich shales. International Journal of Coal Geology 123, 34-51.
Gasparik, M., Ghanizadeh, A., Bertier, P., Gensterblum, Y., Bouw, S., Krooss, B.M., 2012. High-pressure methane sorption isotherms of black shales from the Netherlands. Energy & fuels 26, 4995-5004.
Gregg, S., Sing, K., 1982. W. Adsorption, surface area and porosity. London: Academic Press, 195-197.
Guthrie, J.M., Pratt, L.M., 1994. Geochemical indicators of depositional environment and source-rock potential for the Upper Ordovician Maquoketa Group, Illinois Basin. AAPG bulletin 78, 744-757.
Heller, R., Zoback, M., 2014. Adsorption of methane and carbon dioxide on gas shale and pure mineral samples. Journal of Unconventional Oil and Gas Resources 8, 14-24.
Hu, H., 2014. Methane adsorption comparison of different thermal maturity kerogens in shale gas system. Chinese Journal of Geochemistry 33, 425-430.
Huang, L., Ning, Z., Wang, Q., Zhang, W., Cheng, Z., Wu, X., Qin, H., 2018. Effect of organic type and moisture on CO 2/CH 4 competitive adsorption in kerogen with implications for CO 2 sequestration and enhanced CH 4 recovery. Applied Energy 210, 28-43.
Hunt, J., 1979. Petroleum geochemistry and geology, San Francisco, California.
Ismadji, S., Soetaredjo, F.E., Ayucitra, A., 2015. The Characterization of Clay Minerals and Adsorption Mechanism onto Clays, Clay Materials for Environmental Remediation. Springer, pp. 93-112.
Jarvie, D.M., Hill, R.J., Ruble, T.E., Pollastro, R.M., 2007. Unconventional shale-gas systems: The Mississippian Barnett Shale of north-central Texas as one model for thermogenic shale-gas assessment. AAPG bulletin 91, 475-499.
Ji, L., Zhang, T., Milliken, K.L., Qu, J., Zhang, X., 2012. Experimental investigation of main controls to methane adsorption in clay-rich rocks. Applied Geochemistry 27, 2533-2545.
Ji, W., Song, Y., Jiang, Z., Chen, L., Li, Z., Yang, X., Meng, M., 2015. Estimation of marine shale methane adsorption capacity based on experimental investigations of Lower Silurian Longmaxi formation in the Upper Yangtze Platform, south China. Marine and Petroleum Geology 68, 94-106.
Ji, W., Song, Y., Rui, Z., Meng, M., Huang, H., 2017. Pore characterization of isolated organic matter from high matured gas shale reservoir. International Journal of Coal Geology 174, 31-40.
Jin, Z., Firoozabadi, A., 2014. Effect of water on methane and carbon dioxide sorption in clay minerals by Monte Carlo simulations. Fluid Phase Equilibria 382, 10-20.
Joubert, J.I., Grein, C.T., Bienstock, D., 1973. Sorption of methane in moist coal. Fuel 52, 181-185.

Kuila, U., McCarty, D.K., Derkowski, A., Fischer, T.B., Topór, T., Prasad, M., 2014. Nano-scale texture and porosity of organic matter and clay minerals in organic-rich mudrocks. Fuel 135, 359-373.
Li, J., Li, X., Wang, X., Li, Y., Wu, K., Shi, J., Yang, L., Feng, D., Zhang, T., Yu, P., 2016. Water distribution characteristic and effect on methane adsorption capacity in shale clay. International Journal of Coal Geology 159, 135-154.
Li, J., Zhou, S., Gaus, G., Li, Y., Ma, Y., Chen, K., Zhang, Y., 2018. Characterization of methane adsorption on shale and isolated kerogen from the Sichuan Basin under pressure up to 60 MPa: Experimental results and geological implications. International Journal of Coal Geology 189, 83-93.
Li, W., Pang, X., Snape, C., Zhang, B., Zheng, D., Zhang, X., 2019. Molecular Simulation Study on Methane Adsorption Capacity and Mechanism in Clay Minerals: Effect of Clay Type, Pressure, and Water Saturation in Shales. Energy & Fuels 33, 765-778.
Liming, J., Junli, Q., Tongwei, Z., 2012a. Experiments on methane adsorption of common clay minerals in shale. Earth Science: Journal of China University of Geosciences 37, 1043-1050.
Liming, J., Junli, Q., Yanqing, X., Tongwei, Z., 2012b. Micro-pore characteristics and methane adsorption properties of common clay minerals by electron microscope scanning. Acta Petrolei Sinica 33, 249-256.
Liu, J., Sun, N., Sun, C., Liu, H., Snape, C., Li, K., Wei, W., Sun, Y., 2015. Spherical potassium intercalated activated carbon beads for pulverised fuel CO2 post-combustion capture. Carbon 94, 243-255.
Liu, K., Ostadhassan, M., Zou, J., Gentzis, T., Rezaee, R., Bubach, B., Carvajal-Ortiz, H., 2018. Nanopore structures of isolated kerogen and bulk shale in Bakken Formation. Fuel 226, 441-453.
Loucks, R.G., Reed, R.M., Ruppel, S.C., Hammes, U., 2012. Spectrum of pore types and networks in mudrocks and a descriptive classification for matrix-related mudrock pores. AAPG bulletin 96, 1071-1098.
Loucks, R.G., Reed, R.M., Ruppel, S.C., Jarvie, D.M., 2009. Morphology, genesis, and distribution of nanometer-scale pores in siliceous mudstones of the Mississippian Barnett Shale. Journal of sedimentary research 79, 848-861.
Luffel, D., Guidry, F., 1992. New core analysis methods for measuring reservoir rock properties of Devonian shale. Journal of Petroleum Technology 44, 1,184-181,190.
Ma, L., Fauchille, A.-L., Dowey, P.J., Pilz, F.F., Courtois, L., Taylor, K.G., Lee, P.D., 2017. Correlative multi-scale imaging of shales: a review and future perspectives. Geological Society, London, Special Publications 454, 175-199.
Malik, S., Smith, L., Sharman, J., Holt, E.M., Rigby, S.P., 2016. Pore structural characterization of fuel cell layers using integrated mercury porosimetry and computerized X-ray tomography. Industrial & Engineering Chemistry Research 55, 10850-10859.
Merkel, A., Fink, R., Littke, R., 2016. High pressure methane sorption characteristics of lacustrine shales from the Midland Valley Basin, Scotland. Fuel 182, 361-372.
Milliken, K.L., Rudnicki, M., Awwiller, D.N., Zhang, T., 2013. Organic matter–hosted pore system, Marcellus formation (Devonian), Pennsylvania. AAPG bulletin 97, 177-200.
Pang, Y., Tian, Y., Soliman, M.Y., Shen, Y., 2019. Experimental measurement and analytical estimation of methane absorption in shale kerogen. Fuel 240, 192-205.
Pauling, L., 1935. The structure and entropy of ice and of other crystals with some randomness of atomic arrangement. Journal of the American Chemical Society 57, 2680-2684.
Peng, J., Milliken, K., Fu, Q., Janson, X., Hamlin, S., 2020. Grain assemblages and diagenesis in organic-rich mudrocks, Late Pennsylvanian Cline Shale (Wolfcamp D), Midland Basin, Texas, 2019 AAPG Annual Convention and Exhibition.
Peng, J., Milliken, K.L., Fu, Q., 2019. Quartz types in the Upper Pennsylvanian organic-rich Cline Shale (Wolfcamp D), Midland Basin, Texas: Implications for silica diagenesis, porosity evolution and rock mechanical properties. Sedimentology.

Qi, L., Tang, X., Wang, Z., Peng, X., 2017. Pore characterization of different types of coal from coal and gas outburst disaster sites using low temperature nitrogen adsorption approach. International Journal of Mining Science and Technology 27, 371-377.
Rexer, T.F., Benham, M.J., Aplin, A.C., Thomas, K.M., 2013. Methane adsorption on shale under simulated geological temperature and pressure conditions. Energy & Fuels 27, 3099-3109.
Rexer, T.F., Mathia, E.J., Aplin, A.C., Thomas, K.M., 2014. High-pressure methane adsorption and characterization of pores in Posidonia shales and isolated kerogens. Energy & Fuels 28, 2886-2901.
Ross, D.J., Bustin, R.M., 2007. Shale gas potential of the lower Jurassic Gordondale member, northeastern British Columbia, Canada. Bulletin of Canadian Petroleum Geology 55, 51-75.
Ross, D.J., Bustin, R.M., 2008. Characterizing the shale gas resource potential of Devonian–Mississippian strata in the Western Canada sedimentary basin: Application of an integrated formation evaluation. AAPG bulletin 92, 87-125.
Ross, D.J., Bustin, R.M., 2009. The importance of shale composition and pore structure upon gas storage potential of shale gas reservoirs. Marine and petroleum Geology 26, 916-927.
Rouquerol, J., Llewellyn, P., Rouquerol, F., 2007. Is the BET equation applicable to microporous adsorbents. Stud. Surf. Sci. Catal 160, 49-56.
Ruthven, D.M., 1984. Principles of adsorption and adsorption processes. John Wiley & Sons.
Sing, K.S., 1985. Reporting physisorption data for gas/solid systems with special reference to the determination of surface area and porosity (Recommendations 1984). Pure and applied chemistry 57, 603-619.
Sircar, S., 1999. Gibbsian surface excess for gas adsorption revisited. Industrial & engineering chemistry research 38, 3670-3682.
Tang, L., Song, Y., Jiang, Z., Pang, X., Li, Z., Li, Q., Li, W., Tang, X., Pan, A., 2019. Influencing factors and mathematical prediction of shale adsorbed gas content in the Upper Triassic Yanchang Formation in the Ordos Basin, China. Minerals 9, 265.
Tang, X., Ripepi, N., Stadie, N.P., Yu, L., Hall, M.R., 2016. A dual-site Langmuir equation for accurate estimation of high pressure deep shale gas resources. Fuel 185, 10-17.
Thommes, M., Kaneko, K., Neimark, A.V., Olivier, J.P., Rodriguez-Reinoso, F., Rouquerol, J., Sing, K.S., 2015. Physisorption of gases, with special reference to the evaluation of surface area and pore size distribution (IUPAC Technical Report). Pure and Applied Chemistry 87, 1051-1069.
Wang, S., Javadpour, F., Feng, Q., 2016. Confinement correction to mercury intrusion capillary pressure of shale nanopores. Scientific reports 6, 20160.
Whitelaw, P., Uguna, C.N., Stevens, L.A., Meredith, W., Snape, C.E., Vane, C.H., Moss-Hayes, V., Carr, A.D., 2019. Shale gas reserve evaluation by laboratory pyrolysis and gas holding capacity consistent with field data. Nature communications 10, 1-10.
Xiong, J., Liu, X., Liang, L., Zeng, Q., 2017. Adsorption of methane in organic-rich shale nanopores: An experimental and molecular simulation study. Fuel 200, 299-315.
Young, J.F., 1967. Humidity control in the laboratory using salt solutions—a review. Journal of Applied Chemistry 17, 241-245.
Zhang, T., Ellis, G.S., Ruppel, S.C., Milliken, K., Yang, R., 2012. Effect of organic-matter type and thermal maturity on methane adsorption in shale-gas systems. Organic geochemistry 47, 120-131.
Zhang, Y., Xu, Z., 1995. Atomic radii of noble gas elements in condensed phases. American Mineralogist 80, 670-675.
Zhao, T., Li, X., Ning, Z., Zhao, H., Li, M., 2018. Molecular simulation of methane adsorption on type II kerogen with the impact of water content. Journal of Petroleum Science and Engineering 161, 302-310.
Zhu, Y., Xia, X., 2013. Comparison and explanation of the absorptivity of organic matters and clay minerals in shales. Journal of China Coal Society 38, 812-816.
Zolfaghari, A., Dehghanpour, H., Holyk, J., 2017a. Water sorption behaviour of gas shales: I. Role of clays. International Journal of Coal Geology 179, 130-138.

Zolfaghari, A., Dehghanpour, H., Xu, M., 2017b. Water sorption behaviour of gas shales: II. Pore size distribution. International Journal of Coal Geology 179, 187-195.
Zou, C., Dong, D., Wang, S., Li, J., Li, X., Wang, Y., Li, D., Cheng, K., 2010. Geological characteristics and resource potential of shale gas in China. Petroleum exploration and development 37, 641-653.
Zou, J., Rezaee, R., Liu, K., 2017. Effect of temperature on methane adsorption in shale gas reservoirs. Energy & Fuels 31, 12081-12092.
Zou, J., Rezaee, R., Xie, Q., You, L., Liu, K., Saeedi, A., 2018. Investigation of moisture effect on methane adsorption capacity of shale samples. Fuel 232, 323-332.

Declaration of interests

☒ The authors declare that they have no known competing financial interests or personal relationships that could have appeared to influence the work reported in this paper.

☐The authors declare the following financial interests/personal relationships which may be considered as potential competing interests:
